

Nonreciprocal Second-Harmonic Generation in Few-Layer Chromium Triiodide

Wenshen Song,^{1,*} Ruixiang Fei,^{1,*} and Li Yang^{1,2,†}

¹*Department of Physics, Washington University in St. Louis, St. Louis, MO 63130, USA*

²*Institute of Materials Science and Engineering, Washington University in St. Louis, St. Louis, Missouri 63130, USA*

It is of fundamental importance but challenging to simultaneously identify atomic and magnetic configurations of two-dimensional van der Waals materials. In this work, we show that the nonreciprocal second-harmonic generation (SHG) can be a powerful tool to answer this challenge. Despite the preserved lattice inversion symmetry, the interlayer antiferromagnetic order and spin-orbit coupling generate enhanced SHG in PT-symmetric bilayer chromium triiodide (CrI₃). Importantly, the in-plane polarization-resolved SHG is sensitive to subtly different interlayer structures that cannot be told by linear optical spectra. Beyond bilayer, we further predict that the intensity and angle-resolved SHG can be employed to identify both interlayer atomic and magnetic configurations of trilayer CrI₃. Our first-principles results agree with available measurements and show the potential of SHG as a non-contacting approach to explore correlations between interlayer structures and magnetic orders of emerging ultra-thin magnetic materials.

I. INTRODUCTION

Antiferromagnetic (AFM) materials could represent the future of spintronic applications due to many advanced features, such as robustness against the magnetic-field perturbation, ultrafast dynamics, and large magnetoresistance effects¹⁻³. For example, experimental demonstrations of the electrical switching and detection of the Neel order of AFM CuMnAs open a new avenue towards memory devices based on antiferromagnets⁴. However, simultaneously identifying both AFM order and atomic structures is difficult for conventional magnetometry approaches². This challenge is more serious for emerging two-dimensional (2D) van der Waals (vdW) magnets. Although neutron diffraction plays a major role in probing magnetic orders for bulk crystals⁵, it is not applicable for epitaxial or exfoliated ultra-thin structures because of substrate effects. To date magneto-optics effects, such as the magneto-optics Faraday and Kerr effect, have been widely used for detecting the Neel order of 2D magnets.⁶⁻⁸ Meanwhile, the terahertz radiation, which predominantly interacts with low-energy excitations, is an excellent tool for detecting the spin-wave excitation in magnetic materials. Nevertheless, both probing tools cannot tell the subtle interlayer structural information, which is, however, crucial for studying vdW materials because their magnetic orders are strongly correlated with interlayer configurations.⁹⁻¹¹

Second-harmonic generation (SHG) is a powerful tool to discriminate the magnetic point or space groups that are indistinguishable by the above diffraction methods¹²⁻¹⁵. Particularly, significant nonlinear optical (NLO) responses were reported in bilayer AFM chromium triiodide (CrI₃)^{16,17}, indicating potentially unique SHG of layered magnetic materials. Beyond studying CrI₃, which exhibits a considerable magneto-optics effect¹⁶⁻¹⁹, SHG is also capable in studying those AFM materials that have rather weak magneto-optics effects²⁰. This advantage broadens the applicable range of SHG. Correspondingly, a systematical theoretical

study of SHG and its relationship with interlayer atomic and magnetic orders is crucial for understanding available measurements and motivating further efforts to explore complex symmetries of 2D vdW structures.

In this work, we focus on SHG of bilayer and trilayer CrI₃ using first-principles calculations. Despite the lattice inversion symmetry, the interlayer AFM order and spin-orbit coupling (SOC) of bilayer CrI₃ break both inversion and time-reversal symmetries of magnetic space groups, leading to non-zero SHG signals. We further find that the polarization-resolved azimuthal SHG is determined by the space group of parent lattices and it can be utilized to distinguish the subtle differences between interlayer structures. For trilayer CrI₃, our calculation shows that SHG can tell both interlayer atomic and magnetic orders, giving rise to a powerful tool to efficiently explore symmetries of ultra-thin 2D materials.

The remainder of this work is organized as follows: In Section II, we present the calculation methods and simulation details. In Section III, the lattice structures of CrI₃ and linear optical properties are introduced. In Section IV, we discuss the origin and mechanism of non-vanishing SHG in PT-symmetric systems. In Section V, the SHG susceptibility of bilayer CrI₃ is obtained by first-principles simulations. In Section VI, we show the polarization-resolved SHG and how to utilize it to distinguish different interlayer structures of bilayer CrI₃. In Section VII, we expand the SHG study to trilayer CrI₃ and show how to tell the interlayer atomic and magnetic configurations. Finally, the results are summarized in the conclusion section.

II. CALCULATION DETAILS

We calculate the structural and electronic properties of CrI₃ by density functional theory (DFT) within the generalized gradient approximation (GGA) using the Perdew-Burke-Ernzerhof (PBE) functional²¹, which is implemented in the Vienna *ab initio* simulation package (VASP)^{22,23}. The vdW interactions are included through

the DFT-D3 method with zero dampings^{24,25}. The converged charge densities and wavefunctions are obtained in plane-wave basis with an energy cutoff of 450 eV. SOC is included in all simulations. To deal with localized d orbitals of Cr atoms, the DFT+U scheme is employed with $U = 3$ eV⁹. Our main conclusions of SHG are not sensitive to the value of U .

A k -point sampling of $32 \times 32 \times 1$ is used to obtain converged optical susceptibilities. The linear optical response is calculated based on single-particle interband transitions^{19,26–28}. DFT is known for underestimating band gaps and neglecting many-electron corrections, such as exciton effects^{29,30}. However, in this study, we particularly focus on characters of polarization dependencies of SHG according to symmetries of materials. Therefore, we do not include excitonic effects, and the band gap is corrected by rigidly shifting the DFT band gap to meet the observed lowest-energy exciton peak¹⁹. Within this approximation, the profiles of calculated NLO spectra may not be accurate, but the polarization-symmetry dependence of optical responses shall be reliable due to that electron-hole (e - h) interactions do not break any existing structural/magnetic symmetry. For SHG calculations, we follow the framework of perturbation theory based on the polarization operator³¹ by using the ArchNLO package.²⁷ We include 120 conduction bands for each layer of CrI_3 for converged SHG spectra. Finally, we only consider in-plane optical responses because of the local-field effect that quenches off-plane electric field^{32–34}.

III. ATOMIC STRUCTURES AND LINEAR OPTICAL RESPONSES OF BILAYER AFM CHROMIUM TRIIODIDE

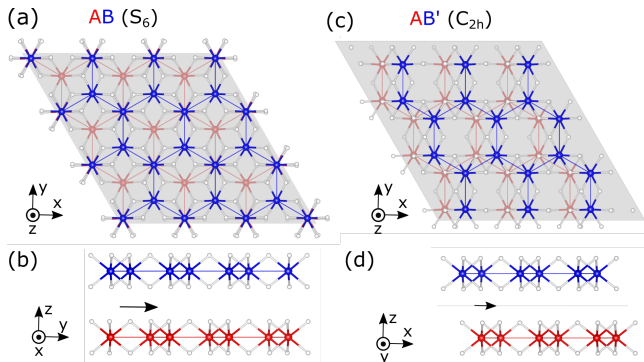


FIG. 1. Top and side views of crystal structures of bilayer CrI_3 . (a) and (b) are the AB stacking structure with a point group S_6 , and it is corresponding to the rhombohedral structure of bulk CrI_3 at low temperature. (c) and (d) are the AB' stacking structure with a point group C_{2h} , and it is corresponding to the monoclinic structure of bulk CrI_3 at high temperature.

Bulk CrI_3 is a layered vdW magnetic material³⁵. Each layer of CrI_3 owns hexagonal lattices in a D_{3d} point

group, in which magnetic Cr atoms form a honeycomb structure and each Cr atom is surrounded by six I atoms. A unit cell of bulk CrI_3 can be obtained by stacking three monolayers following the ABC-Bernal configuration with the same interlayer translation. There are two observed interlayer structures³⁶. One is formed by a $[1/3, 1/3]$ interlayer shift, and it is observed at temperature below 210 K, called the low-temperature (LT) structure. The other one is formed by a $[1/3, 0]$ interlayer shift, and it is observed at temperature above 210 K, called the high-temperature (HT) structure^{36,37}.

The corresponding bilayer structures and symmetry groups based these two bulk phases are presented in Figs. 1 (a)-(d), in which the AB stacking style is from the bulk LT phase while the AB' stacking style is from the bulk HT phase. In this work, we mainly focus on the interlayer AFM order because of two reasons: 1) the interlayer AFM order has been widely observed in intrinsic 2D samples³⁸; 2) the inversion symmetry is preserved in FM bilayer CrI_3 , and only the AFM order exhibits non-zero SHG.

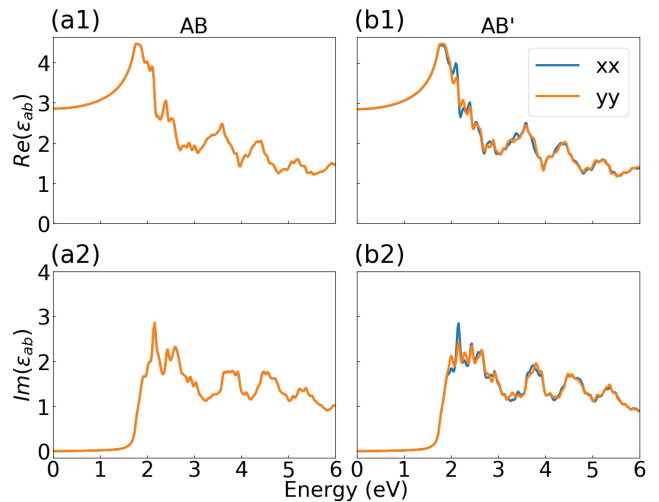


FIG. 2. Real and imaginary parts of the in-plane linear dielectric functions of AFM bilayer CrI_3 . (a1) and (a2) are those of the AB interlayer structure. (b1) and (b2) are those of the AB' interlayer structure.

The DFT-calculated real and imaginary parts of the linear dielectric function are plotted in Fig. 2 for the AB and AB' interlayer structures, respectively. Both AB and AB' interlayer structures exhibit nearly identical linear dielectric responses, except for a few minor differences. The AB stacking shows a perfectly isotropic linear dielectric function, where the xx and yy components are the same. This isotropy is essentially decided by its S_6 point group. On the other hand, the spectra of the AB' stacking exhibit a minor anisotropy because of its lower-symmetric C_{2h} point group. However, this difference is too small to be detected in practical linear optical spectra. Needless to say that the linear dielectric function may not be an efficient way to tell interlayer structures

of bilayer CrI_3 .

IV. ORIGIN OF SHG IN PARITY-TIME SYMMETRIC AFM SYSTEMS

Before presenting the first-principles SHG simulation results, it is necessary to introduce general expressions and discuss the origin of non-zero SHG signals in interlayer AFM vdW systems, which keep the parity-time (PT) symmetry.

Following previous works,^{31,39} the SHG susceptibility $\chi_{abc}^{(2)}(-2\omega; \omega, \omega)$ can be generally expressed as

$$\chi_{abc}^{(2)}(-2\omega; \omega, \omega) = \chi_{II}^{abc}(-2\omega; \omega, \omega) + \eta_{II}^{abc}(-2\omega; \omega, \omega) + \sigma_{II}^{abc}(-2\omega; \omega, \omega). \quad (1)$$

Specifically, the interband transitions at the same crystal momentum \mathbf{k} contribute to

$$\chi_{II}^{abc}(-2\omega; \omega, \omega) = \frac{e^3}{\hbar^2} \sum_{nml} \int \frac{d\mathbf{k}}{8\pi^3} \frac{r_{nm}^a r_{ml}^b r_{ln}^c}{\omega_{ln} - \omega_{ml}} \times \left(\frac{f_{ml}}{\omega_{ml} - \omega} + \frac{f_{ln}}{\omega_{ln} - \omega} + \frac{2f_{nm}}{\omega_{mn} - 2\omega} \right). \quad (2)$$

The modulation of the linear susceptibility due to intraband motions of electrons contributes to

$$\eta_{II}^{abc}(-2\omega; \omega, \omega) = \frac{e^3}{\hbar^2} \int \frac{d\mathbf{k}}{8\pi^3} \left\{ \sum_{nml} \omega_{mn} r_{nm}^a \{ r_{ml}^b r_{ln}^c \} \left[\frac{f_{nl}}{\omega_{ln}^2 (\omega_{ln} - \omega)} + \frac{f_{lm}}{\omega_{ml}^2 (\omega_{ml} - \omega)} \right] - 8i \sum_{nm} \frac{f_{nm} r_{nm}^a}{\omega_{mn}^2 (\omega_{mn} - 2\omega)} \{ \Delta_{mn}^b r_{mn}^c \} - \frac{2 \sum_{nml} f_{nm} r_{nm}^a \{ r_{ml}^b r_{ln}^c \} (\omega_{ln} - \omega_{ml})}{\omega_{mn}^2 (\omega_{mn} - 2\omega)} \right\}. \quad (3)$$

Finally, the term describing the modification by the polarization energy associated with interband motions contributes to

$$\sigma_{II}^{abc}(-2\omega; \omega, \omega) = \frac{e^3}{2\hbar^2} \int \frac{d\mathbf{k}}{8\pi^3} \left\{ \sum_{nml} \frac{f_{nm}}{\omega_{mn}^2 (\omega_{mn} - \omega)} \left[\omega_{nl} r_{lm}^a \{ r_{mn}^b r_{nl}^c \} - \omega_{lm} r_{nl}^a \{ r_{lm}^b r_{mn}^c \} \right] + i \sum_{nm} \frac{f_{nm} r_{nm}^a}{\omega_{mn}^2 (\omega_{mn} - 2\omega)} \{ \Delta_{mn}^b r_{mn}^c \} \right\} \quad (4)$$

In Eq. 1~4, we define the momentum matrix element, $p_{ij}^a = \langle kj | \hat{p}_a | ki \rangle$, as the transition between two states i and j at the same \mathbf{k} point, and the position matrix element is defined by $r_{nm}^a(\mathbf{k}) = \frac{p_{nm}^a(\mathbf{k})}{im\omega_{nm}}$ if $n \neq m$ or 0 if

$n = m$. Meanwhile, $\{ r_{ml}^b r_{ln}^c \} \equiv \frac{1}{2} (r_{ml}^b r_{ln}^c + r_{ml}^c r_{ln}^b)$ and $\Delta_{mn}^b \equiv \frac{p_{mm}^b(\mathbf{k}) - p_{nn}^b(\mathbf{k})}{m_e}$ (m_e is the electron mass).

It is known that the SHG response is zero in centrosymmetric materials if time-reversal symmetry is preserved. This can be understood from the above formulas, in which the $r_{nm} r_{ml} r_{ln}$ and $r_{nm} r_{ml} \Delta_{ln}$ terms are odd under inversion symmetry. As a result, their integrations over reciprocal space are zero. However, if considering the magnetic order, the inversion symmetry of the magnetic space group may be broken even with a preserved lattice inversion symmetry, giving hope to non-zero SHG.

In both AB and AB' AFM bilayer CrI_3 , the lattices own the inversion symmetry. However, because the space inversion operator cannot reverse the spin-degree freedom, the inversion symmetry in the magnetic space group is broken. Interestingly, this symmetry breaking itself does not guarantee non-zero SHG. Particularly, due to PT symmetry, the spin-up and spin-down band structures are degenerated, and they are symmetric in reciprocal space because of the $SU(2)$ spin-rotation symmetry⁴⁰. For example, Fig. 3 (a) shows this symmetric band structure of AFM AB bilayer CrI_3 . As a result, the SHG response is zero because the intraband group velocity is odd in reciprocal space due to these symmetric band structures.

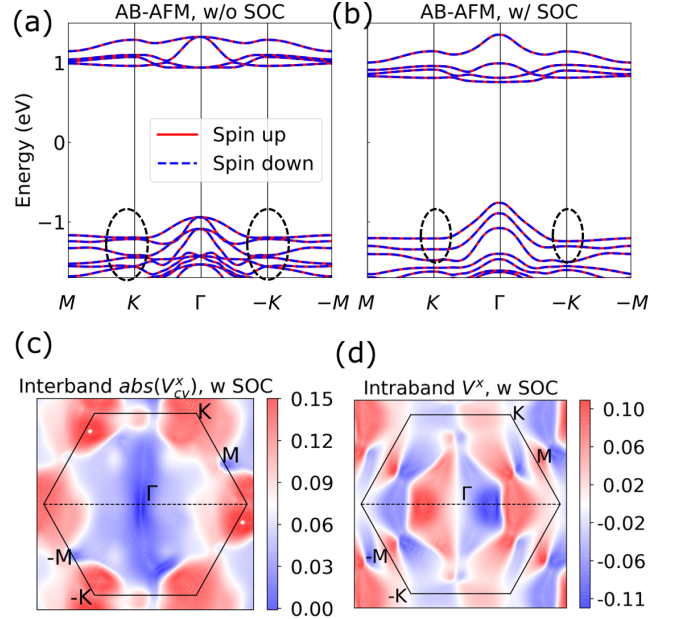


FIG. 3. (a) Band structure of AFM AB bilayer CrI_3 without SOC included. (b) is that with SOC included. The Fermi level is set to be at the middle of the band gap. (c) The distribution of the interband velocity matrix between the lowest conduction and highest valence bands in reciprocal space. (d) The distribution of the intraband velocity matrix of the lowest conduction band in reciprocal space.

Fortunately, SOC is known to be strong in CrI_3 , and it breaks the $SU(2)$ spin-rotation symmetry^{17,41}. To

demonstrate the symmetry breaking, we plot the band structure with SOC included for the AFM AB bilayer structure in Fig. 3 (b). Black dotted circles are marked around K and $-K$ points to address the broken symmetric band structures by SOC. Moreover, as shown in Figs. 3 (c) and (d), the parity symmetries of both interband and intraband velocity matrices, which are calculated by first-principles simulations, are also broken with SOC included. Because the strength of SHG susceptibility is proportional to the integral of transition intensity and velocity matrices in reciprocal space, these asymmetric velocity matrices indicate non-zero SHG.

V. SHG SUSCEPTIBILITY OF BILAYER AFM CHROMIUM TRIIODIDE

The in-plane components of SHG susceptibility tensor have been calculated, and those nonzero components are plotted in Figs. 4 (a1) and (b1) for AFM AB and AB' bilayer CrI₃, respectively. Unlike the similar linear optical spectra in Fig. 2, those NLO SHG spectra exhibit significant differences between two interlayer structures. Figure 4 (a1) presents that there are two non-zero independent SHG spectra for the AB interlayer structure, and each contains three degenerated components. The dark-blue line represents the absolute SHG susceptibility elements of degenerated $\chi_{112}^{(2)} = \chi_{211}^{(2)} = -\chi_{222}^{(2)}$, while the cyan line represents those of degenerated $\chi_{111}^{(2)} = -\chi_{122}^{(2)} = \chi_{212}^{(2)}$. In the AB' stacking case shown in Fig. 4 (b1), there are three non-zero independent SHG spectra, $\chi_{112}^{(2)}$, $\chi_{211}^{(2)}$, and $\chi_{222}^{(2)}$ because of the lower symmetry.

To help analyze the spectra of SHG susceptibilities, we plot the double-frequency linear optical absorption spectra ($Im(\epsilon_x(2\omega))$) in Figs. 4 (a2) and (b2) of both interlayer structures. This is an approximation to only consider two-photon processes with identical energy, reflecting the double-photon resonance.^{27,42} Interestingly, the profiles of double-resonant spectra and the significant component of SHG spectra are similar. For example, the first significant peak in the spectrum of $\chi_{112}^{(2)}$ is at 1.1 eV. It agrees well with the first peak of $Im(\epsilon_x(2\omega))$, as shown in Fig. 4 (a2). Such a phenomenon indicates that main features (peaks) of SHG spectra are dominated by double-resonance processes. This is consistent with previous studies on transition-metal dichalcogenides and hybrid halide perovskites^{27,42}.

It is important to notice that the amplitude of SHG susceptibility of bilayer PT-symmetric CrI₃ structures is significant. As shown in Fig. 4, their values can reach $7 \times 10^4 \text{ pm}^2/V$. These magnetic-ordering induced SHG signals are comparable to those of monolayer MoS₂ ($1 \times 10^4 \text{ pm}^2/V \sim 6 \times 10^4 \text{ pm}^2/V$), which owns a non-centrosymmetric structure^{28,43-47}. Moreover, the SHG signals of bilayer AFM CrI₃ are about one order of magnitude larger than those of a hexagonal boron nitride (h -BN) sheet ($0.1 \times 10^4 \text{ pm}^2/V \sim 0.6 \times 10^4 \text{ pm}^2/V$)^{28,43,44}.

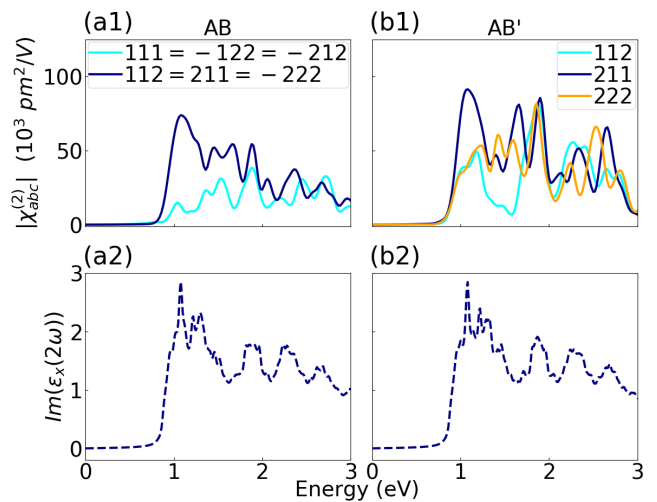


FIG. 4. (a1) SHG spectra of the in-plane SHG susceptibility ($|\chi_{abc}^{(2)}|$) of AFM AB bilayer CrI₃. (b1) are those of AFM AB' bilayer CrI₃. The subscripts, 1, 2, and 3, denote the Cartesian coordinates x , y , and z . (a2) and (b2) are the imaginary part of the double-resonant dielectric function $\epsilon_x(2\omega)$ of AB and AB' bilayer CrI₃, respectively.

This enhanced SHG agrees with recent measurements of bilayer CrI₃¹⁶.

VI. POLARIZATION-RESOLVED SHG OF BILAYER CHROMIUM TRIIODIDE

Although SHG spectra of AB and AB' interlayer structures are different, it is not convenient to directly use them to identify structures because this approach needs data of a wide range of frequencies. A more efficient approach is to measure the polarization-resolved SHG at a fixed frequency of the excitation beam^{16,48,49}. In the following, we adopt the popular experimental setup and give the angle-resolved SHG polarization of bilayer AFM CrI₃^{16,28}. The response direction is set to be parallelly (co-linearly) or perpendicularly (cross-linearly) polarized with respect to the azimuthal polarization of incident beam. Meanwhile, we keep these two directions rotating together within the xy plane.

The electric field of incident light is given by

$$\begin{cases} E_x = E \cos\theta \\ E_y = E \sin\theta, \end{cases} \quad (5)$$

in which x, y donate laboratory coordinates, and θ represents the azimuthal rotational angle. E_x and E_y are Cartesian components of the electric field of incident light.

In this work, we assume a normal incidence and focus on the in-plane detection and excitation. The response

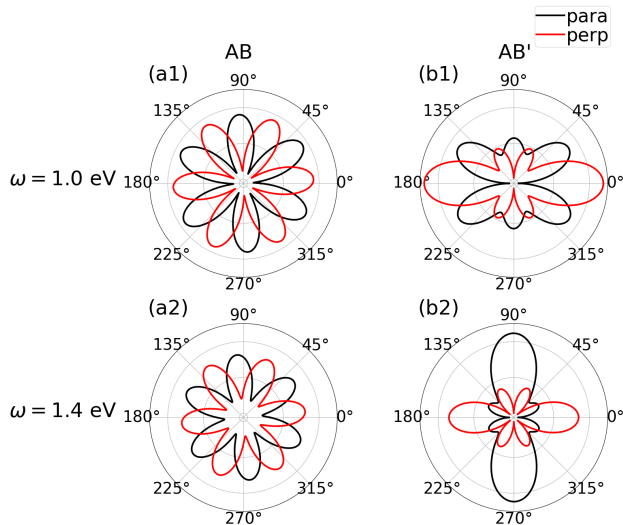


FIG. 5. Polarization-resolved SHG of AFM bilayer CrI_3 . ω represents the energy of incident photons, and para (perp) represents the parallel (perpendicular) polarization component. (a1) and (a2) are those of the AB stacking with incident photon at 1.0 eV and 1.4 eV, respectively. (b1) and (b2) are those of the AB' stacking.

of in-plane SHG polarization is given by

$$\begin{cases} P_x = \chi_{111}^{(2)} E_x^2 + 2\chi_{112}^{(2)} E_x E_y + \chi_{122}^{(2)} E_y^2 \\ P_y = \chi_{211}^{(2)} E_x^2 + 2\chi_{212}^{(2)} E_x E_y + \chi_{222}^{(2)} E_y^2. \end{cases} \quad (6)$$

$\chi_{abc}^{(2)}$ presents components of SHG tensors, in which the subscripts (1,2, and 3) donate x , y , and z . The first subscript is the response direction, and the last two are the excitation directions. P_x and P_y are induced polarizations by excitation electric fields.

Finally, the parallel (perpendicular) SHG polarization can be defined as

$$\begin{cases} P_{\parallel} = P_x \cos\theta + P_y \sin\theta \\ P_{\perp} = -P_x \sin\theta + P_y \cos\theta, \end{cases} \quad (7)$$

in which $\parallel(\perp)$ indicates the parallel (perpendicular) polarization component.

Figure 5 shows the polarization dependence of SHG responses for AB and AB' stackings of AFM bilayer CrI_3 at two fixed frequencies ($\omega=1.0$ eV and 1.4 eV). Unlike linear optical responses shown in Fig. 2, the in-plane polarization-resolved SHG is sensitive to the subtle interlayer structures. In Figs. 5 (a1) and (a2) of the AB stacking AFM bilayer CrI_3 , both para and perp SHG signals exhibit a 6-fold sunflower-like pattern. On the contrary, for the AB' stacking, the SHG patterns exhibit a butterfly-like two-fold mirror symmetry, as shown in Figs. 5 (b1) and (b2).

These patterns are essentially decided by the symmetry groups of interlayer structures. For the AB-type bilayer which owns a high-symmetry S_6 point group, the 3-fold

rotation symmetry results in: $\chi_{111}^{(2)} = -\chi_{122}^{(2)} = \chi_{212}^{(2)}$ as well as $\chi_{112}^{(2)} = \chi_{211}^{(2)} = -\chi_{222}^{(2)}$ (indicated in Fig. 4 (a1)). We can substitute these formulas into Eqs. 5~7. The parallel and perpendicular SHG susceptibilities are reduced to be

$$\begin{cases} \chi_{\parallel} = \chi_{111}^{(2)} \cos 3\theta + \chi_{112}^{(2)} \sin 3\theta \\ \chi_{\perp} = -\chi_{111}^{(2)} \sin 3\theta + \chi_{112}^{(2)} \cos 3\theta. \end{cases} \quad (8)$$

Therefore, the absolute value of parallel and perpendicular polarizations exhibit a 6-fold symmetry due to the $\cos 3\theta$ and $\sin 3\theta$ terms. Such a 6-fold SHG pattern has also been observed in similarly three-fold-symmetry structures, such as monolayer MoS_2 and $h\text{-BN}$ ^{28,49-53}.

For the AB' stacking structure with a C_{2h} symmetry, the distinct non-zero in-plane elements of the SHG susceptibility tensor are $\chi_{112}^{(2)}$, $\chi_{211}^{(2)}$, and $\chi_{222}^{(2)}$, as shown in Fig. 4 (b1). In this case, the parallel and perpendicular SHG polarization components are reduced to be

$$\begin{cases} \chi_{\parallel} = (2\chi_{112}^{(2)} + \chi_{211}^{(2)}) \sin\theta \cos^2\theta + \chi_{222}^{(2)} \sin^3\theta \\ \chi_{\perp} = (-2\chi_{112}^{(2)} + \chi_{222}^{(2)}) \sin^2\theta \cos^2\theta + \chi_{211}^{(2)} \cos^3\theta. \end{cases} \quad (9)$$

These formulas of polarization components are complicated, leading to the more anisotropic polarization-resolved SHG. However, the absolute values are even-parity according to the angle (θ), resulting in a two-fold mirror symmetry, as shown in Figs. 5 (b1) and (b2). These characteristic mirror-symmetry patterns of the polarization-resolved SHG have been also observed in monolayer group-IV monochalcogenides²⁸ because of their same point group.

These distinct features of polarization-resolved SHG in Fig. 5 make it easy to distinguish interlayer structures of bilayer AFM CrI_3 . In fact, the similarly polarization-resolved SHG shown in Figs. 5 (b1) and (b2) were observed in fabricated bilayer CrI_3 with 1000-nm incident light, confirming the AB' (HT) interlayer structure¹⁶. This observed AB' (HT) bilayer is surprising because the structural phase transition temperature of bulk CrI_3 is around 210 K³⁶, which is substantially higher than the temperature (~ 5 K) measuring SHG of bilayer structures. It will be valuable to explore the fundamental reason for the preserved HT phase of ultra-thin CrI_3 structures at low temperatures.

VII. LINEAR OPTICAL RESPONSES AND SHG OF TRILAYER CHROMIUM TRIIODIDE

We focus on two stable interlayer configurations, i.e., the ABA and AB'A stacking styles of trilayer CrI_3 . Unlike bilayer, both FM and AFM orders break the inversion symmetry of the magnetic group of trilayer CrI_3 , resulting in non-zero SHG. It is worth mentioning that, although most available measurements observed an interlayer AFM order in few-layer CrI_3 , a few recent studies

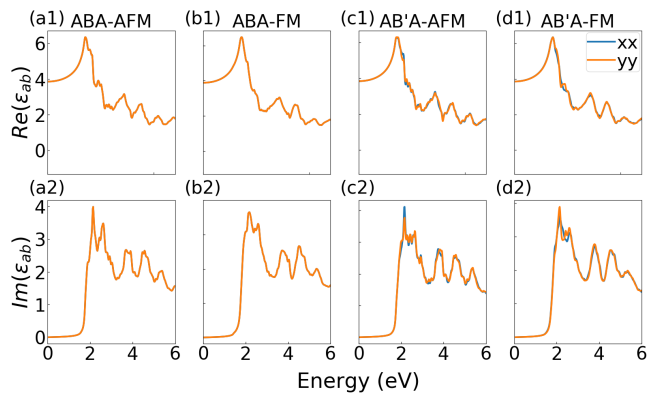


FIG. 6. (a1) and (a2) are real and imaginary parts of the in-plane linear dielectric functions of ABA-AFM trilayer CrI_3 , respectively. (b1) and (b2) are those of ABA-FM trilayer CrI_3 . (c1) and (c2) are those of AB'A-AFM trilayer CrI_3 . (d1) and (d2) are those of AB'A-FM trilayer CrI_3 .

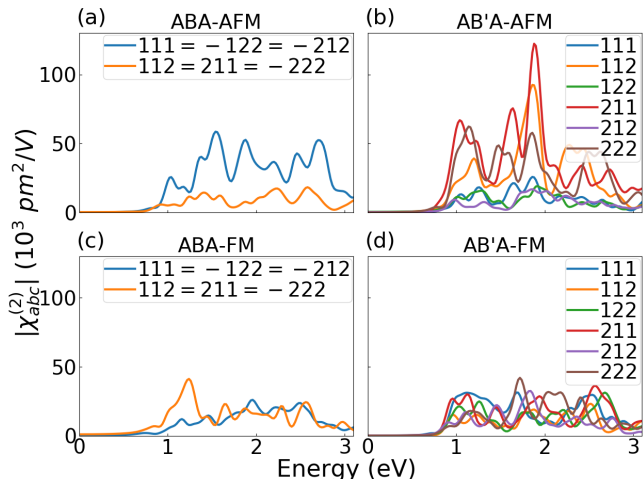


FIG. 7. (a) SHG spectra of the in-plane SHG susceptibility ($|\chi_{abc}^{(2)}|$) of ABA-AFM trilayer CrI_3 . (b) Those of AB'A-AFM trilayer CrI_3 . (c) Those of ABA-FM trilayer CrI_3 . (d) Those of AB'A-FM trilayer CrI_3 . The subscripts, 1, 2, and 3, denote the Cartesian coordinates x , y , and z .

show that external factors, such as pressure, can switch the interlayer magnetic ordering efficiently¹⁰. Therefore, we will calculate SHG of both interlayer AFM and FM orders of trilayer structures.

Figure 6 presents the real and imaginary parts of the linear dielectric function of ABA and AB'A configurations with FM and AFM orders, respectively. Like those of bilayer structures, the linear optical spectra of trilayer CrI_3 are nearly identical for different interlayer structures and magnetic orders. Because of the lower symmetry of the AB'A interlayer structure, its linear spectra are slightly anisotropic. Unfortunately, these minor differences may not be significant enough to identify structural and magnetic orders for trilayer CrI_3 .

Figures 7 (a)-(d) presents the SHG spectra of trilayer

CrI_3 with different interlayer structures and magnetic orders. As expected, interlayer magnetic and atomic configurations strongly affect SHG responses. The ABA stacking style has two independent components for both FM and AFM, which are similar with the bilayer case shown in Fig. 4 (a1), indicating a good preservation of symmetries. The AB'A stacking style has six independent non-zero components, due to its lower symmetry. Other than the different profiles of SHG spectra, we can observe that the spectra of AFM structures have more significant peaks and their average SHG intensities are also higher than those of FM structures. This may provide an opportunity to identify magnetic orders of trilayer CrI_3 .

Following the same analysis stated in Section VI, we have further calculated the polarization-resolved SHG patterns of trilayer CrI_3 , which are plotted in Fig. 8. Two typical excitation frequencies ($\omega=1.0$ eV and 1.4 eV) are considered in these figures. In these angle-resolved cases, the SHG polarization is more sensitive to the interlayer atomic structures than the magnetic order. For example, for the ABA stacking style, both AFM and FM orders exhibit a 6-fold sunflower-like pattern, which is similar to the case of AB stacked bilayer. For the AB'A stacking style, both FM and AFM orders exhibit distorted butterfly-like patterns, which are similar to the bilayer AB' case but with a lower symmetry. We also notice that the intensity of SHG polarizations of the AFM order is usually stronger than those of the FM order. This is consistent with the observations of Fig. 7. As a result, the polarization pattern of SHG is effective to tell the crystal structures while its intensity may be useful to tell the magnetic order.

VIII. CONCLUSION

In summary, we have shown that the nontrivial AFM order and SOC break the inversion symmetry and lead to enhanced SHG signals in PT-symmetric bilayer CrI_3 . Different patterns of polarization-resolved azimuthal SHG can be utilized to distinguish the AB and AB' interlayer structures. We further expand this approach to discover both magnetic and interlayer structures of trilayer CrI_3 . The overall intensity of SHG signals can be used to identify magnetic orders, and the polarization-resolved SHG is effective to distinguish interlayer crystal structures. Our calculation provides understandings of recent measurements and sheds light on using nonlinear light-matter interactions to explore atomic and magnetic structures of ultra-thin 2D vdW materials.

ACKNOWLEDGMENTS

This work is supported by the National Science Foundation (NSF) CAREER grant No. DMR-1455346, NSF EFRI2DARE-1542815, and the Air Force Office of Sci-

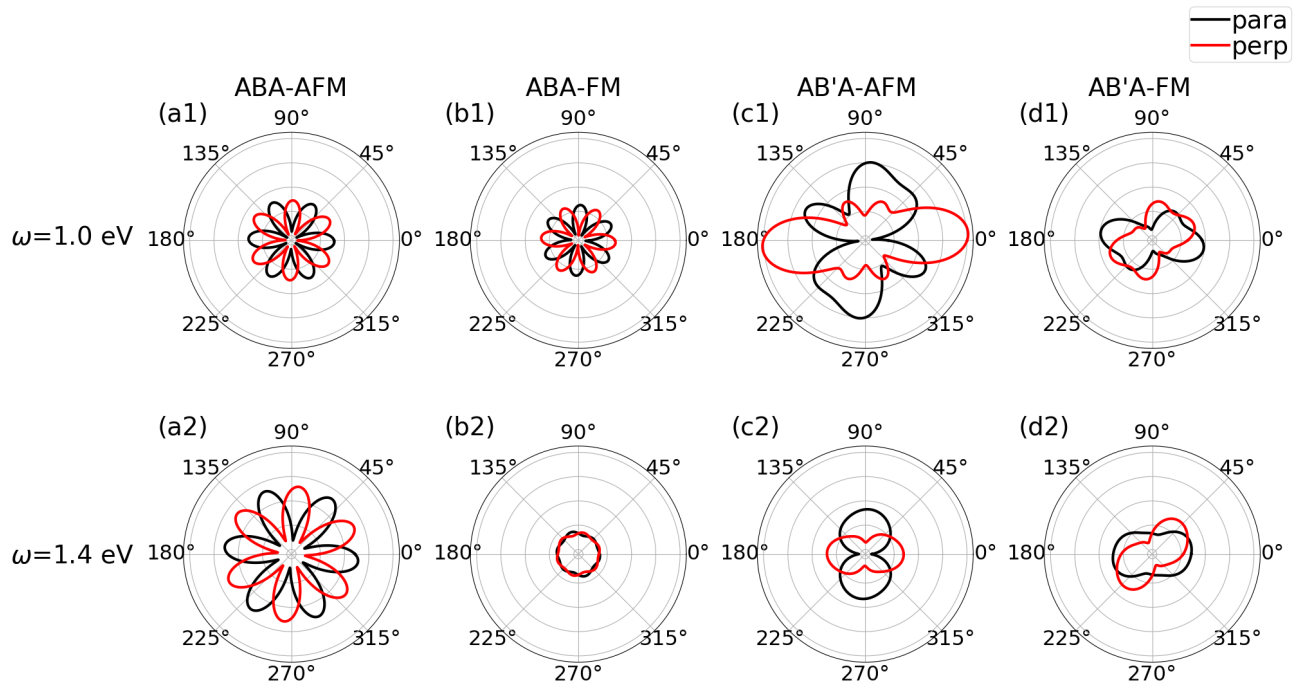


FIG. 8. Polarization-resolved SHG of trilayer CrI_3 . ω represents energy of incident photons, and para (perp) represents the parallel (perpendicular) polarization component. (a1) and (a2) are those of the ABA-AFM trilayer CrI_3 with incident photon at 1.0 eV and 1.4 eV, respectively. (b1) and (b2) are those of the ABA-FM trilayer CrI_3 . (c1) and (c2) are those of the AB'A-AFM trilayer CrI_3 . (d1) and (d2) are those of the AB'A-FM trilayer CrI_3 .

entific Research (AFOSR) grant No. FA9550-17-1-0304. The computational resources are provided by the Stam-

pede of Teragrid at the Texas Advanced Computing Center (TACC) through XSEDE.

* These authors contributed equally to this work.

† lyang@physics.wustl.edu

¹ V. Baltz, A. Manchon, M. Tsoi, T. Moriyama, T. Ono, and Y. Tserkovnyak, *Reviews of Modern Physics* **90**, 015005 (2018).

² P. Němec, M. Fiebig, T. Kampfrath, and A. V. Kimel, *Nature Physics* **14**, 229 (2018).

³ Z. Wang, I. Gutiérrez-Lezama, N. Ubrig, M. Kroner, M. Gibertini, T. Taniguchi, K. Watanabe, A. Imamoglu, E. Giannini, and A. F. Morpurgo, *Nature communications* **9**, 1 (2018).

⁴ P. Wadley, B. Howells, J. Elezny, C. Andrews, V. Hills, R. P. Campion, V. Novak, K. Olejnik, F. Maccherozzi, S. S. Dhesi, S. Y. Martin, T. Wagner, J. Wunderlich, F. Freimuth, Y. Mokrousov, J. Kune, J. S. Chauhan, M. J. Grzybowski, A. W. Rushforth, K. W. Edmonds, B. L. Gallagher, and T. Jungwirth, *Science* **351**, 587 (2016).

⁵ C. G. Shull, W. Strauser, and E. Wollan, *Physical Review* **83**, 333 (1951).

⁶ K. L. Seyler, D. Zhong, D. R. Klein, S. Gao, X. Zhang, B. Huang, E. Navarro-Moratalla, L. Yang, D. H. Cobden, M. A. McGuire, *et al.*, *Nature Physics* **14**, 277 (2018).

⁷ W. Chen, Z. Sun, Z. Wang, L. Gu, X. Xu, S. Wu, and C. Gao, *Science* **366**, 983 (2019).

⁸ K. F. Mak, J. Shan, and D. C. Ralph, *Nature Reviews Physics* **1**, 646 (2019).

⁹ N. Sivadas, S. Okamoto, X. Xu, C. J. Fennie, and D. Xiao, *Nano letters* **18**, 7658 (2018).

¹⁰ T. Li, S. Jiang, N. Sivadas, Z. Wang, Y. Xu, D. Weber, J. E. Goldberger, K. Watanabe, T. Taniguchi, C. J. Fennie, *et al.*, *Nature materials* **18**, 1303 (2019).

¹¹ S. W. Jang, M. Y. Jeong, H. Yoon, S. Ryee, and M. J. Han, *Phys. Rev. Materials* **3**, 031001 (2019).

¹² M. Fiebig, D. Fröhlich, K. Kohn, T. Lottermoser, V. Pavlov, R. Pisarev, *et al.*, *Physical review letters* **84**, 5620 (2000).

¹³ M. Fiebig, V. V. Pavlov, and R. V. Pisarev, *JOSA B* **22**, 96 (2005).

¹⁴ S. Ju, T.-Y. Cai, C.-I. Wei, and G.-Y. Guo, *Opt. Lett.* **34**, 3860 (2009).

¹⁵ M. Lucking, K. Beach, and H. Terrones, *Sci. Rep.* **8**, 10118 (2018).

¹⁶ Z. Sun, Y. Yi, T. Song, G. Clark, B. Huang, Y. Shan, S. Wu, D. Huang, C. Gao, Z. Chen, M. McGuire, T. Cao, D. Xiao, W.-T. Liu, W. Yao, X. Xu, and S. Wu, *Nature* **572**, 497 (2019).

¹⁷ Y. Zhang, T. Holder, H. Ishizuka, F. de Juan, N. Nagaosa, C. Felser, and B. Yan, *Nature Communications* **10**, 1 (2019).

- ¹⁸ V. K. Gudelli and G.-Y. Guo, *New Journal of Physics* **21**, 053012 (2019).
- ¹⁹ M. Wu, Z. Li, T. Cao, and S. G. Louie, *Nature communications* **10**, 1 (2019).
- ²⁰ J. Wang, C. Sun, Y. Hashimoto, J. Kono, G. A. Khodaparast, L. Cywiński, L. Sham, G. D. Sanders, C. J. Stanton, and H. Munekata, *Journal of Physics: Condensed Matter* **18**, R501 (2006).
- ²¹ J. P. Perdew, K. Burke, and M. Ernzerhof, *Physical Review Letters* **77**, 3865 (1996).
- ²² G. Kresse and J. Furthmüller, *Physical review B* **54**, 11169 (1996).
- ²³ G. Kresse and D. Joubert, *Physical Review B* **59**, 1758 (1999).
- ²⁴ S. Grimme, J. Antony, S. Ehrlich, and H. Krieg, *The Journal of Chemical Physics* **132**, 154104 (2010).
- ²⁵ S. Grimme, S. Ehrlich, and L. Goerigk, *Journal of computational chemistry* **32**, 1456 (2011).
- ²⁶ G. Guo, K. Chu, D.-s. Wang, and C.-g. Duan, *Physical Review B* **69**, 205416 (2004).
- ²⁷ W. Song, G.-Y. Guo, S. Huang, L. Yang, and L. Yang, *Phys. Rev. Applied* **13**, 014052 (2020).
- ²⁸ H. Wang and X. Qian, *Nano Letters* **17**, 5027 (2017).
- ²⁹ R. Fei, L. Z. Tan, and A. M. Rappe, *Phys. Rev. B* **101**, 045104 (2020).
- ³⁰ Y.-H. Chan, D. Y. Qiu, F. H. da Jornada, and S. G. Louie, *arXiv preprint arXiv:1904.12813* (2019).
- ³¹ J. L. P. Hughes and J. E. Sipe, *Physical Review B* **53**, 10751 (1996).
- ³² T. Ando, *Journal of the Physical Society of Japan* **66**, 1066 (1997).
- ³³ M. Machón, S. Reich, C. Thomsen, D. Sánchez-Portal, and P. Ordejón, *Physical Review B* **66**, 155410 (2002).
- ³⁴ A. Marinopoulos, L. Reining, A. Rubio, and N. Vast, *Physical review letters* **91**, 046402 (2003).
- ³⁵ L. Handy and N. Gregory, *Journal of the American Chemical Society* **74**, 891 (1952).
- ³⁶ M. A. McGuire, H. Dixit, V. R. Cooper, and B. C. Sales, *Chemistry of Materials* **27**, 612 (2015).
- ³⁷ P. Jiang, C. Wang, D. Chen, Z. Zhong, Z. Yuan, Z.-Y. Lu, and W. Ji, *Phys. Rev. B* **99**, 144401 (2019).
- ³⁸ B. Huang, G. Clark, E. Navarro-Moratalla, D. R. Klein, R. Cheng, K. L. Seyler, D. Zhong, E. Schmidgall, M. A. McGuire, D. H. Cobden, *et al.*, *Nature* **546**, 270 (2017).
- ³⁹ C. Aversa and J. Sipe, *Physical Review B* **52**, 14636 (1995).
- ⁴⁰ R. S. Mong, A. M. Essin, and J. E. Moore, *Physical Review B* **81**, 245209 (2010).
- ⁴¹ R. Fei, W. Song, and L. Yang, *arXiv:2003.01576* (2019).
- ⁴² C.-Y. Wang and G.-Y. Guo, *The Journal of Physical Chemistry C* **119**, 13268 (2015).
- ⁴³ M. Grüning and C. Attaccalite, *Phys. Rev. B* **89**, 081102 (2014).
- ⁴⁴ Y. Li, Y. Rao, K. F. Mak, Y. You, S. Wang, C. R. Dean, and T. F. Heinz, *Nano letters* **13**, 3329 (2013).
- ⁴⁵ N. Kumar, S. Najmaei, Q. Cui, F. Ceballos, P. M. Ajayan, J. Lou, and H. Zhao, *Phys. Rev. B* **87**, 161403 (2013).
- ⁴⁶ L. M. Malard, T. V. Alencar, A. P. M. Barboza, K. F. Mak, and A. M. de Paula, *Phys. Rev. B* **87**, 201401 (2013).
- ⁴⁷ M. L. Trolle, G. Seifert, and T. G. Pedersen, *Phys. Rev. B* **89**, 235410 (2014).
- ⁴⁸ E. I. Romijn, A. Finnøy, R. Kumar, and M. B. Lilledahl, *PLoS one* **13** (2018).
- ⁴⁹ F. Yang, W. Song, F. Meng, F. Luo, S. Lou, S. Lin, Z. Gong, J. Cao, E. Bernard, E. Chan, L. Yang, and J. Yao, submitted (2019).
- ⁵⁰ N. Kumar, S. Najmaei, Q. Cui, F. Ceballos, P. M. Ajayan, J. Lou, and H. Zhao, *Physical Review B* **87**, 161403 (2013).
- ⁵¹ L. M. Malard, T. V. Alencar, A. P. M. Barboza, K. F. Mak, and A. M. de Paula, *Physical Review B* **87**, 201401 (2013), *arXiv:1304.4289*.
- ⁵² Y. Li, Y. Rao, K. F. Mak, Y. You, S. Wang, C. R. Dean, and T. F. Heinz, *Nano Letters* **13**, 3329 (2013).
- ⁵³ W.-T. Hsu, Z.-A. Zhao, L.-J. Li, C.-H. Chen, M.-H. Chiu, P.-S. Chang, Y.-C. Chou, and W.-H. Chang, *ACS Nano* **8**, 2951 (2014).